Lawrence Berkeley National Laboratory

Title
System integration and performance of the EUV engineering test stand

Permalink
https://escholarship.org/uc/item/60n3d1hf

Authors
Tichenor, Daniel A.
Ray-Chaudhuri, Avijit K.
Replogle, William C.
et al.

Publication Date
2001-03-01

System Integration and Performance of the EUV Engineering Test Stand

Daniel A. Tichenor[*a], Avijit K. Ray-Chaudhuri[a], William C. Replogle[a],
Richard H. Stulen[a], Glenn D. Kubiak[a], Paul D. Rockett[a], Leonard E. Klebanoff[a],
Karen L. Jefferson[a], Alvin H. Leung[a], John B. Wronosky[b], Layton C. Hale[c],
Henry N. Chapman[c], John S. Taylor[c], James A. Folta[c], Claude Montcalm[c],
Regina Soufli[c], Eberhard Spiller[c], Kenneth Blaedel[f], Gary E. Sommargren[c],
Donald W. Sweeney[c], Patrick Naulleau[d], Kenneth A. Goldberg[d], Eric M. Gullikson[d],
Jeffrey Bokor[d], Phillip J. Batson[d], David T. Attwood[d], Keith H. Jackson[d],
Scott D. Hector[e], Charles W. Gwyn[f], and Pei-Yang Yan[f],

[a]Sandia National Laboratories, PO Box 969, Livermore CA 94551
[b]Sandia National Laboratories, PO Box 5800, Albuquerque NM 87185
[c]Lawrence Livermore National Laboratory, PO Box 808, Livermore, CA 94550
[d]Lawrence Berkeley National Laboratory, One Cyclotron Road, Berkeley, CA 94720
[e]Motorola Corporation, 3501 Ed Bluestein Blvd, Austin TX 78721
[f]Intel Corporation, 2200 Mission College Boulevard, Santa Clara CA 95052

ABSTRACT

The Engineering Test Stand (ETS) is a developmental lithography tool designed to demonstrate full-field EUV imaging and provide data for commercial-tool development. In the first phase of integration, currently in progress, the ETS is configured using a developmental projection system, while fabrication of an improved projection system proceeds in parallel. The optics in the second projection system have been fabricated to tighter specifications for improved resolution and reduced flare. The projection system is a 4-mirror, 4x-reduction, ring-field design having a numeral aperture of 0.1, which supports 70 nm resolution at a k_1 of 0.52. The illuminator produces 13.4 nm radiation from a laser-produced plasma, directs the radiation onto an arc-shaped field of view, and provides an effective fill factor at the pupil plane of 0.7. The ETS is designed for full-field images in step-and-scan mode using vacuum-compatible, magnetically levitated, scanning stages. This paper describes system performance observed during the first phase of integration, including static resist images of 100 nm isolated and dense features.

Keywords: EUVL, lithography, multilayer coatings, optical fabrication, optical design, laser-produced plasma, laser plasma source, maglev, magnetic levitation, stages, precision engineering

1. INTRODUCTION

During the past year Extreme Ultraviolet Lithography (EUVL) has become widely viewed as the leading next-generation-lithography candidate for dense features down to 30 nm with introduction as early as the 70 nm node. An alpha-class tool, called the EUV Engineering Test Stand (ETS), has been developed to demonstrate full-field printing of EUV images and to develop the system learning required to commercialize EUVL technology[1]. The ETS is designed to meet the system learning objectives at critical dimensions in the 70 nm to 100 nm range. In a parallel effort, a micro-exposure tool[2] (MET) is being developed to study EUV imaging down to 30 nm and provide a test bed for resist development. Advancement in multilayer coatings for 13.4 nm radiation is the enabling technology that supports all-reflective projection systems for the ETS and production tools designed to operate in step-and-scan mode. EUVL technology development is funded by the EUV Limited Liability Company (LLC), a consortium of semiconductor manufacturers founded in 1997 and comprised of Advanced Micro Devices, Infineon, Intel, IBM, Micron, and Motorola. The Department of Energy Virtual National Laboratory, comprised of Lawrence Berkeley National Laboratory, Lawrence Livermore National Laboratory and Sandia National Laboratories, perform research, development, and engineering to accelerate the commercialization of EUVL.

The Virtual National Laboratory has been working to an accelerated schedule during the past year with the objective of bringing the ETS on line six months ahead of the originally planned operation date. The ETS has completed the subsystem-qualification and system-assembly phases and is currently operational in static imaging mode. Tool-setup parameters, such

_____

* Correspondence: Email: datiche@sandia.gov; Telephone: 925 294 2137; Fax: 925 294 3870

as exposure time, stage skew, scan magnification and focal plane location, are being determined by printing static images and characterizing the results using scanning electron microscopy and high-resolution wafer metrology. This paper reviews progress during the past year in the supporting technologies, subsystem development, and system integration. Initial results from tool-setup experiments in which 100 nm isolated and dense features are printed in photoresist are described.

2. ETS DESIGN AND INTEGRATION

2.1 System design overview

The ETS is comprised of two major environmental enclosures, the source chamber that houses the laser-produced plasma (LPP) source and illumination system, and the main chamber that houses the projection optics and stage system (See Fig. 1). The EUV radiation is generated by focusing a pulsed Nd:YAG laser beam onto a xenon-cluster target, which is supported by a xenon re-circulation system. A six-channel condenser collects radiation from the source and directs it into the main chamber, where a final condenser element shapes the beam to illuminate the arc-shaped field of view of the projection system. A membrane-type spectral-purity filter removes out-of-band radiation and provides an environmental barrier between the source and main chambers.
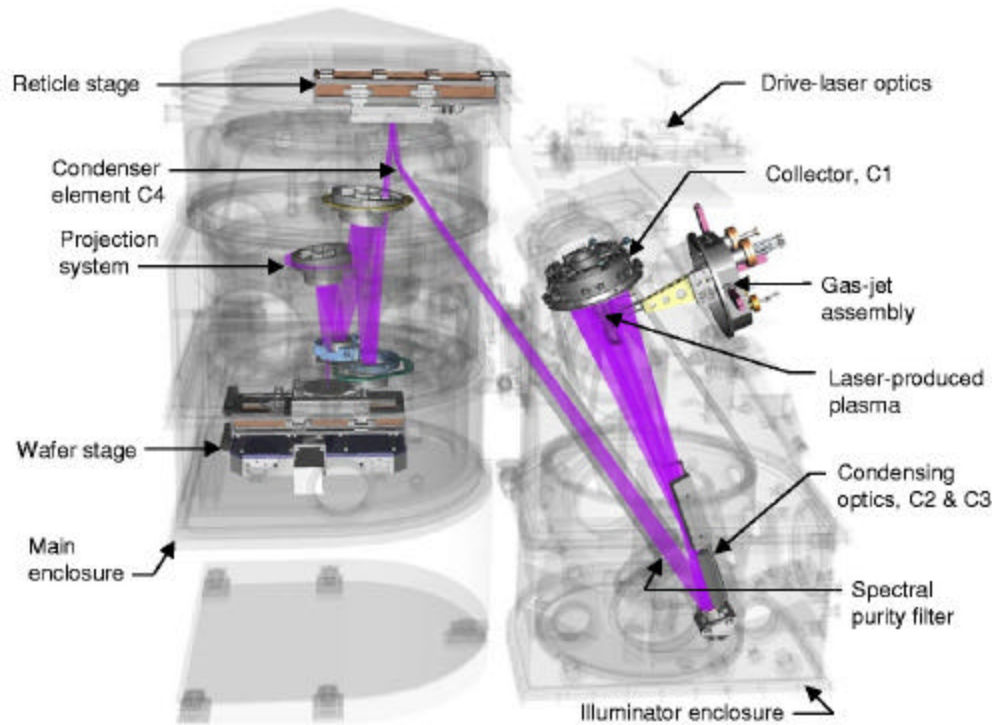

Figure 1. Solid model of the EUV Engineering Test Stand.

The projection system is a 4-mirror, 4x-reduction system having a numerical aperture of 0.1 and is designed for printing full-field images in step-and-scan mode. This design is capable of printing 70 nm dense features at a k_1 value of 0.52. The current phase of ETS integration and characterization uses a developmental projection system, while the final projection system is being assembled and aligned in parallel for installation later this year.

The scanning stage system provides a full 6-degrees of freedom for both the wafer and reticle using magnetic levitation (maglev) technology. A linear motor drives one axis of each stage in the scanning direction, while a set of magnetic actuators enables control of the remaining 5 degrees of freedom over short travel ranges. In the cross-scan direction, a mechanical lead-screw-driven stage provides the travel range needed to cover all sites on a 200 mm wafer. A system of capacitive sensors and laser gauges feeds back the actuator gaps and stage position required for the digital control system to execute stage movements and to maintain stage synchronization. Vacuum compatible vibration isolators support the projection

system and stage metrology, while grounded structures support the reticle and wafer stage bases. The levitated reticle and wafer platens are isolated from ground vibrations through feedback control.

2.2 System integration

Development and testing of the three major subsystems, illuminator, projection optics box, and stages, were performed in parallel prior to integration. The illuminator, comprised of the source, a multi-element condenser and an environmental enclosure, was assembled in its final location in the ETS laboratory and tested in place using a 40 watt, Coherent Infinity Nd:YAG laser. The resulting EUV illumination beam was directed into a diagnostic chamber in which the illumination at the reticle plane and projection-system pupil plane were measured and characterized. ETS integration is progressing using this source, while the high-power source, driven by a 1700 watt TRW Inc. Nd:YAG laser, is being developed in parallel. The capability to operate with either laser has been implemented to facilitate source-power upgrade.

The projection system was assembled and aligned using a developmental set of aspheric mirrors. This projection system, PO Box 1, is installed in the ETS for initial system learning, while the final projection system, PO Box 2, containing mirrors that meet the ETS specifications, is being assembled and tested. PO Box 1 has undergone extensive testing at the actinic wavelength[3].

The wafer and reticle stages were tested with their respective metrology systems on alignment stations designed to verify mechanical alignment and test stage control hardware and software. For each stage the metrology system, comprised of the metrology laser, distance-measuring interferometers, and associated beam splitters and beam benders, were installed and aligned on structures called metrology trays. In the ETS the metrology trays are referenced to each other through a low-expansion structure called the isolated frame.

The main chamber was assembled and characterized in a space adjacent to the ETS laboratory while the illuminator was undergoing testing. The structural components, including the polymer-concrete pedestal, the stage bridge that supports the reticle stage, the vibration isolation system, and the isolated frame, were installed using mass surrogates for the metrology trays and the PO Box to achieve the design weight of 1090 Kg (2400 pounds) required for the coil-spring passive isolators. In this configuration the vibration isolation system performance was tested in the passive/active isolation mode (See Fig. 2).
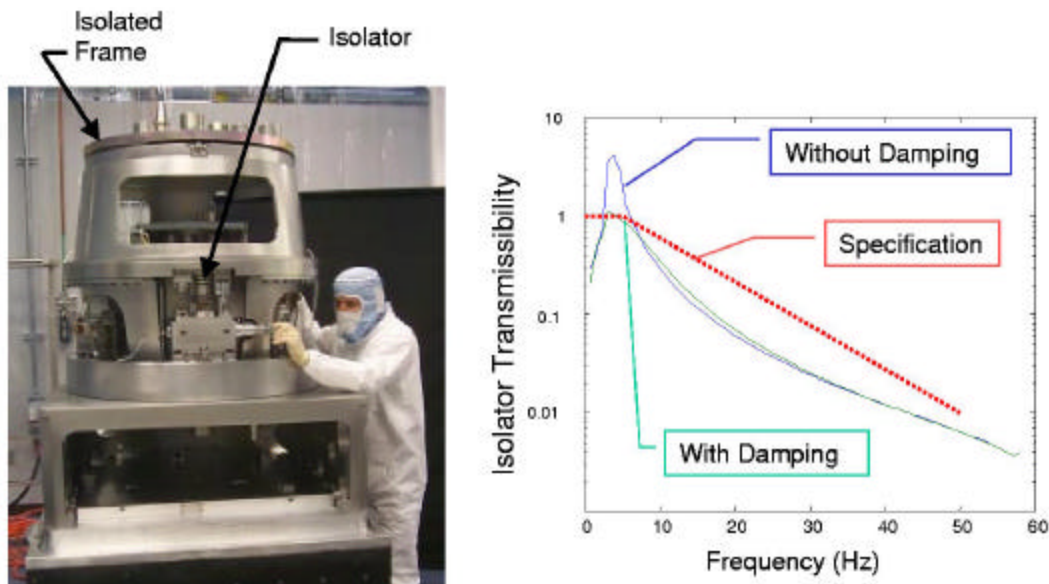

Figure 2. Vibration isolation system installed. Transmissibility curves show improved performance with active damping.

The PO Box was installed through the top hatch of the main chamber, engaging the isolated frame by means of a kinematic interface. Object and image plane sensors, comprised of six capacitance gauges and two video microscopes, define the desired locations of the reticle and wafer planes, respectively, as determined during the final alignment procedure. The reticle stage and metrology tray were installed through the top hatch, and the wafer stage and metrology tray were installed through a side port, using kinematic mounts for all four components. System alignment procedures were performed to adjust the stages and isolated frame to bring the reticle and wafer planes into alignment with the PO Box as determined by the

object and image plane sensors. Kinematic mounts enable the removal and re-installation of the PO Box and stage components without the need to repeat the system alignment. Customized handling equipment was designed and built to facilitate the installation of these components.

The ETS is extensively equipped with sensors to collect data in support of the system-learning role. Approximately 62 temperature sensors, 23 vibration sensors and 21 EUV flux sensors are installed in the ETS. In addition, the ETS contains a number of custom sensors, including source position sensors, a Through-The-Lens Imager (TTLI), an aperture viewing sensor, a reticle dose sensor array, a wafer dose sensor and an Aerial Image Monitor (AIM). The TTLI comprises a visible-light illuminator, custom microscope lens and an external video camera (See Fig. 3). The TTLI illuminator couples light from a remote mercury-arc lamp into an optical fiber that carries the light to an illuminator lens mounted on the main chamber. The light is injected through an optical port and reflects off a moveable folding mirror that is inserted upstream of the C4 mirror. Following the EUV path, the visible light beam reflects off the reticle, and the PO Box casts an image of the reticle onto the wafer. Light reflecting off the wafer is intercepted by a scraper mirror, located 75 mm above the wafer, and directed to the TTLI imaging lens, which then casts the superimposed image of the reticle and wafer through an optical port to an external video camera. The resultant image is shown in Figure 3. This system is used to verify system alignment, locate features on the reticle, and to perform coarse alignment between reticle and wafer.
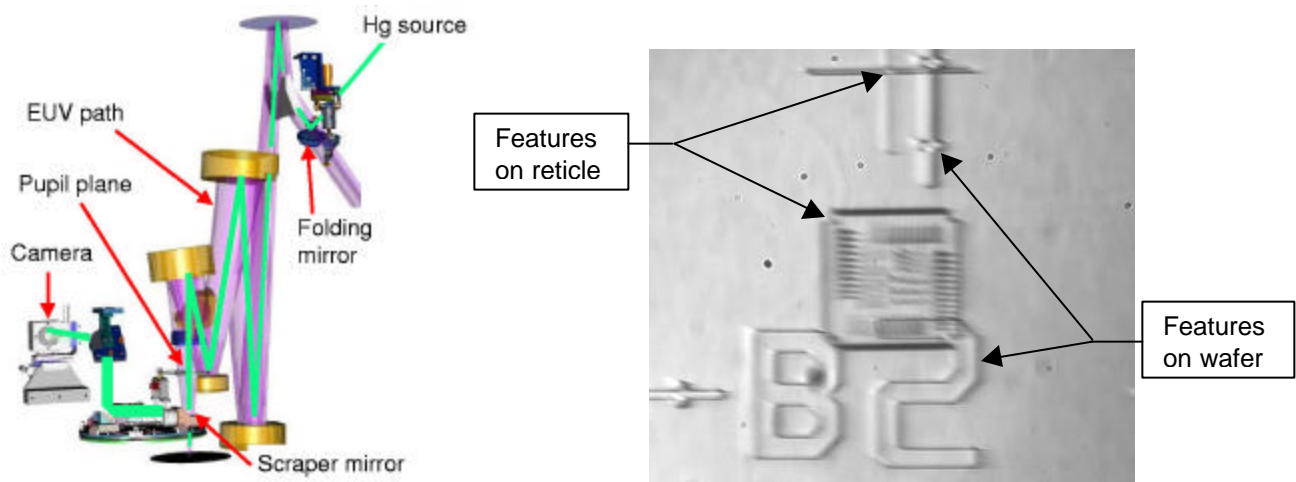

Figure 3. A schematic of the TTLI (left). Superimposed image of reticle and wafer features acquired in the ETS using the TTLI (right).

An aperture viewing system provides images of the EUV fill profile at the pupil of the PO Box. This diagnostic is used to characterize the fill profile and to perform final alignment of the illuminator. The pupil image is obtained by using an in-vacuum actuator to insert a scintillating screen of gadolinium oxysulfide into the EUV path just above the PO Box aperture stop on the M3 mirror. EUV radiation falling on the scintillating screen produces a visible-light image that is viewed through a mirror, located above the scintillating screen and to the side of the EUV path. The image is acquired using a video camera, which views the scintillating screen through an optical port in the main chamber.

EUV sensors located on the wafer and reticle stages perform measurements of dose uniformity at the wafer and reticle plane. In addition, an AIM sensor can be used to characterize projection-system and stage performance. These sensors are based on an EUV-sensitive photodiode, coated with zirconium to eliminate out-of-band radiation. On the reticle stage, a one-dimensional array of 80 photodiodes is scanned through the field of view to acquire an image of the reticle illumination. On the wafer stage a single photodiode is used in each of two sensors, the dose sensor and the AIM sensor, which can be positioned in a two-dimensional field. These sensors are identical except for the EUV-transparent artifact located above the photodiode. A 25 micron pinhole is used for the wafer dose sensor, and a series of narrow slits is used in the AIM sensor to analyze small features imaged from the reticle. For all of these sensors, the EUV signals are acquired and digitized inside electrically shielded enclosures on board the stages to mitigate electromagnetic interference from the plasma source. The data is transmitted digitally to the external sensor controller after the source pulse interference has decayed.

After completion of stage performance testing in the main chamber, the stages and PO Box were removed, and the main chamber assembly was transported into the ETS laboratory using air castors (see Fig. 4). A system alignment procedure was performed to bring the two chambers into alignment and to assure that the illumination beam is incident on the well-corrected

field of view of the PO Box. In the new location a number of diagnostic tests were performed to verify stages-to-PO Box alignment, vibration-isolation system performance, stage system performance, TTLI alignment and vacuum system functionality.
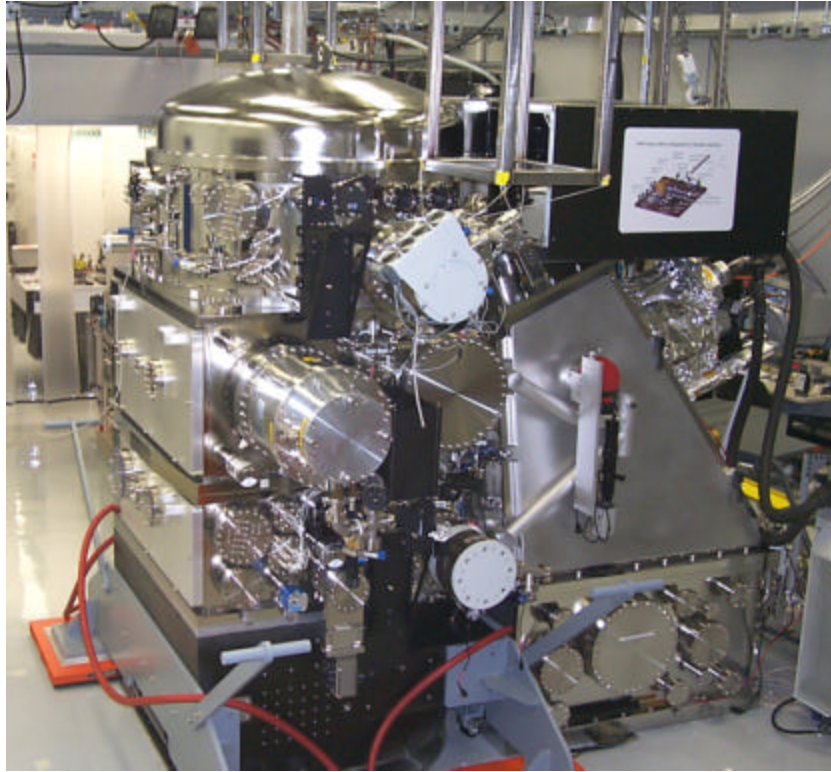

Figure 4. The main chamber (left) being aligned to the source chamber (right).

After these tests were completed, the wafer robot was installed and taught the wafer loading position, thus providing the capability to load and unload wafers without breaking vacuum. The additional controls functionality required for initial tool-setup experiments was implemented, including the acquisition of data from the aperture viewing system, TTLI, temperature sensors and vibration sensors. The initial functionality also includes the acquisition of flux data from in-band detectors located at the first condenser element, C1, and from EUV mirrors throughout the system, which carry a 10 volt negative bias and operate as photo-emission detectors. Finally, the function of moving the stage to positions for focus-exposure matrices was implemented together with the ability to execute static exposures while controlling dose by counting pulses or by integrating the flux measured at the final condenser element, C4.

3. ENVIRONMENTAL SUBSYSTEM

The first environmental data from the ETS has been collected and is shown in Figure 5 for the "Optic Zone" of the Main Chamber. Excellent control of high-mass hydrocarbons has been achieved. This control is a result of extensive outgas testing and screening of components and materials to minimize high mass (>44 amu) hydrocarbons. Furthermore, attention was paid to vacuum compatible design of the ETS, careful cleaning of parts, pre-baking of cables and subassemblies where possible, and clean assembly procedures. As a result of the hydrocarbon control, the residual ETS vacuum environment is rich in water vapor, as indicated in Figure 5. Analysis of witness plate data indicates that the ETS environment does not pose a contamination risk to the optics in the absence of EUV irradiation. However, with EUV exposure, the water rich environment can lead to EUV-induced water oxidation of the Si-terminated Mo/Si optics. It was found that added ethanol can prevent optic oxidation, allowing carbon growth via EUV "cracking" of low-level residual hydrocarbons. The EUV environmental issues are understood, mitigation approaches have been validated, and EUV optic contamination appears to be manageable. Further data concerning the ETS environment can be found in the paper by Klebanoff et al. in these proceedings[4].
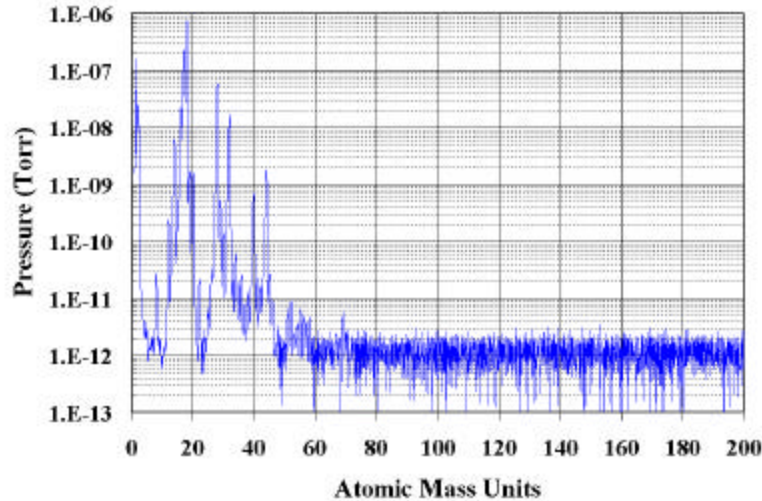
Figure 5. A residual gas analyzer (RGA) spectrum of the optic zone environment. Partial pressure (Torr) is plotted against atomic mass (amu).

4. ILLUMINATOR SUBSYSTEM

The Engineering Test Stand requires a high-power source of EUV light to achieve the desired EUV throughput. Work has proceeded on the development of a laser-produced plasma source of EUV radiation, using a jet stream of Xe as the target.[5-7] Presently, the ETS utilizes a continuous cluster-jet based upon the supersonic expansion of Xe gas into vacuum, a nozzle which was initially produced by Advanced Energy Systems Inc.[5] A 250 mm focal length lens focuses the laser beam from a Coherent Infinity Nd:YAG laser of 4 ns pulse length and 400 mJ energy onto the gas jet, producing an EUV source of roughly 300 microns in diameter. The jet is not cooled and the conversion efficiency is approximately 0.1%, which is sufficient to perform initial imaging experiments. A Xe recirculation system collects the exhausted Xe both immediately following the exit nozzle and from the general chamber pumps and filters and recompresses the gas to pressures of 200-300 psi (Figure 6). This minimizes the amount of Xe used during operation of ETS, and limits the build-up of oxygen, water, and/or hydrocarbons in the Illuminator.
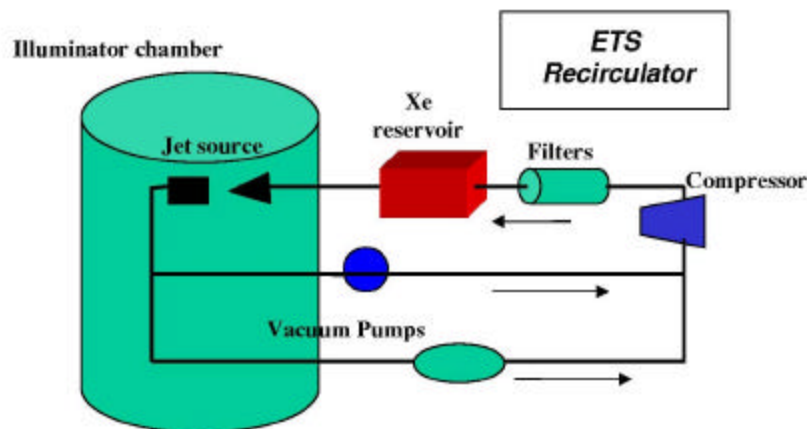

Figure 6.   Schematic of the ETS xenon recirculation system for the EUV jet source.

To attain the required EUV source power and EUV throughput, the TRW Inc. Nd:YAG laser has been directed into ETS for use with a second-generation jet nozzle. The laser delivers on target 1500 W of 1.06 micron light at repetition rates of either

1667 Hz or 5000 Hz with an 8 ns pulse length. Its beam is derived from three largely independent modules which may be multiplexed together to deliver pulses of approximately 300 mJ at 5 kHz, or synchronized higher energy pulses of 900 mJ at 1.667 kHz. Beam focal spot size is near diffraction limited and the stability of its pointing and power level has been excellent, usually less than 0.8% rms deviation. A switchyard optical configuration permits use of either the Coherent or the TRW laser in the ETS.

Advanced Xe jet development has the goal of producing a near-solid density target for a laser-produced plasma source. Earlier experiments at Sandia demonstrated that solid Xe is capable of yielding a conversion efficiency of 1.2%. Thus if a liquid jet of Xe is demonstrated, the near-solid density stream should be capable of achieving conversion efficiencies of at least 1%. In pursuit of that goal two jet nozzles have been developed that utilize increasing levels of cooling to produce a narrow stream of liquified Xe as a laser-target. The first nozzle is referred to as a dewpoint nozzle, because the pressure and temperature of the exiting stream are adjusted so as to drop just below the dewpoint of xenon. The Xe gas is operated at high pressure (300-400 psi) and is cooled to below its dewpoint within a few centimeters of the exit nozzle. Figure 7 shows the dewpoint jet operating in a test chamber and discharging its effluent into a diffuser, which captures the unused Xe and returns it through a closed loop recirculation system. This assures that the background Xe pressure in the Illuminator is maintained below 4 mTorr, minimizing absorption of the 13.4 nm light over the long path (~1 m) to the spectral-purity filter. The filter acts as a vacuum window for the EUV, isolating the main chamber from the Illuminator.
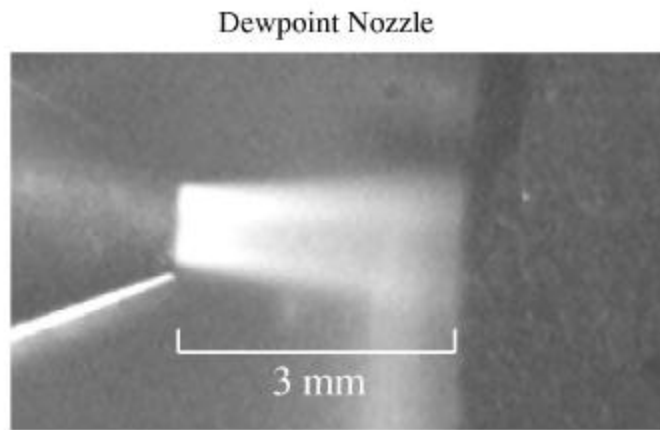

Figure 7. Graphite dewpoint nozzle operating with xenon.

The second advanced jet design incorporates a more effective heat exchanger to fully liquify the gas before reaching the nozzle. This system is operated at lower temperatures than the dewpoint jet and exits through a low aspect ratio pinhole. It produces a long, continuous stream of apparently fully liquid Xe, much like water exiting a garden hose.[8] Its diameter is as small as the pinhole, which in this case is 50 microns, and its length is well over 10 mm. The advantage of a long steady stream is the possibility of illuminating the jet with the laser as far from the nozzle as possible. Magnified images of the un-irradiated jet are seen in Figure 8. The EUV radiation generated in the stream heats the nozzle and can change the fluid characteristics as the laser is operated at several thousand Hertz. Nozzles have been fabricated out of graphite to enhance nozzle thermal conductivity and to minimize deposition of eroded nozzle material on the first condenser C1, thus minimizing the reduction of mirror reflectance. The high thermal loading produced by the uncollected EUV that strikes the nozzle is substantial, requiring significant thermal engineering of this nozzle to assure robust performance at full operation.

Figure 8. Magnified image of 50 micron diameter liquid xenon filament jet (First frame at pinhole exit, second frame 2 mm downstream, third frame 8 mm downstream)

The conversion efficiency obtained with the dewpoint jet was 0.5% at a distance of 1.5 mm from the nozzle. Preliminary measurements on the filament jet indicate a conversion of about 0.6% at a distance of 2.5 mm from the nozzle, already demonstrating the advantages of the liquid jet. Additionally, the source of EUV from the filament jet is at least a factor of two smaller than that emitted in the dewpoint jet. Thus for the present condenser configuration, the etendue of the condenser excludes some of the light produced by the dewpoint jet, but will include all of the EUV light produced in the filament jet.
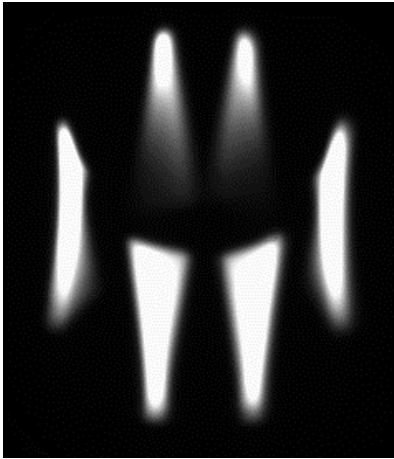
4.2 Condenser

Figure 9. EUV image of the composite pupil fill for all field points as recorded using the pupil viewing system.

EUV radiation from the LPP is collected by six C1 elements that surround the drive laser beam (See Fig. 1). Each collector element focuses the EUV radiation into an arc-shaped field, which is rotated by a grazing-incidence C2 element and a near-normal C3 element to illuminate the well-corrected field of view of the projection system. A final C4 element images the pupil pattern at C3 into the pupil of the projection system, forming a fill profile comprised of six elongated spots which can be viewed using the aperture viewing system. An image of the fill profile in the projection system pupil as shown in Fig. 9. Image simulations indicate that this fill profile, in combination with projection-mirror aberrations, causes significant bias between dense lines orientated vertically compared to those orientated horizontally. In an upgraded condenser design, a scatter plate, integral to C4, will achieve a fill profile that closely approximates the imaging performance of a conventional pupil fill.

5. STAGE SUBSYSTEM

The magnetically levitated stage system[1] is in the final phase of qualification for ETS operations. The wafer and reticle stage each control 5 degrees of freedom over short travel ranges plus one long-travel degree of freedom in the scanning direction. Both stages have demonstrated jitter between 2 nm and 6 nm rms in static operation at all stage positions.

The wafer and reticle stage subsystem consists of maglev reticle and wafer stages, metrology for each stage, and control electronics. A feedback control system provides synchronization of the reticle and wafer stages during exposures. The wafer stage must track the reticle stage during scanning of the reticle stage through the EUV field. Throughput, structural stability, critical dimension, and wafer exposure characteristics determine stage subsystem specifications for acceleration, scan speed, settle time, and dynamic stability. The ETS requires that jitter for each stage as referenced to the PO box always be
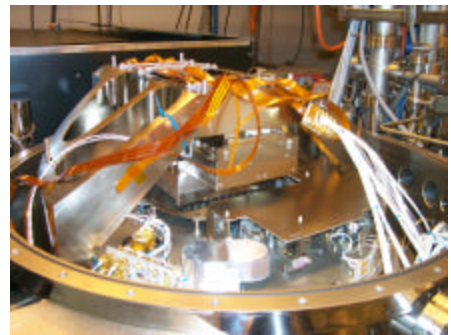

Figure 10. ETS reticle stage.

less than 10 nm rms and that the mean tracking error be less than ±3nm[9]. Performance to these specifications has been demonstrated in the ETS. Figures 10 and 11 show the reticle and wafer stages installed in the ETS.

5.1 Stage subsystem progress during 2000

Since first operation of the development wafer stage in late 1999, the EUV program has integrated the vacuum-compatible wafer and reticle stages into the ETS. Fabrication and installation of the stage computer control system and electronics has been completed. Changes have been made to both the stage hardware and the control electronics and software to incorporate knowledge gained through operation and analysis.

The stage concept was modified to accommodate an accelerated ETS testing schedule and performance issues relating to the cable stage design. The cable stage is included in the overall design concept to minimize position disturbances caused by cable forces seen by the platen. The cable stage has been removed for early imaging. This is possible due to reduced scanning velocity requirements for first imaging experiments. Corrections to the design will be implemented over the next year.

Electrical noise concerns dictated greater attention to signal management in the control electronics. The evolution includes custom VME bus signal management and custom signal conditioning for the high-speed (MHz) position measurement electronics.
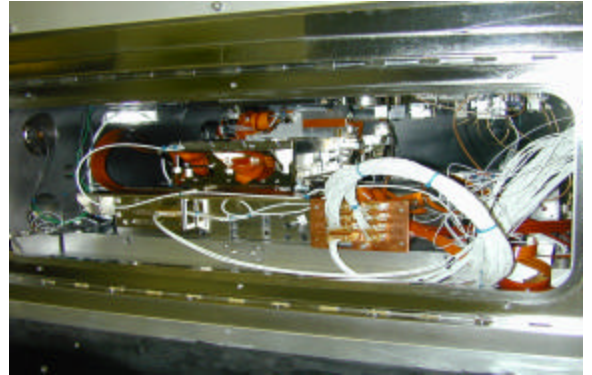

Figure 11. ETS wafer stage.

5.2 Performance results

Evaluation of the stage performance in the ETS for first imaging experiments has been completed. The results are acceptable for positioning of the reticle and wafer for EUV imaging. Both static and scanning performance measurements are shown. Figure 12 shows static jitter of each stage over its travel range. Figure 13 represents the combination of the wafer and reticle stage jitter and can be used to predict image blur. Figures 14 and 15 show scanning performance of the development wafer stage operating without the cable stage at velocities required for early imaging experiments. Stage and system performance will evolve with ongoing system analysis and operational experience.
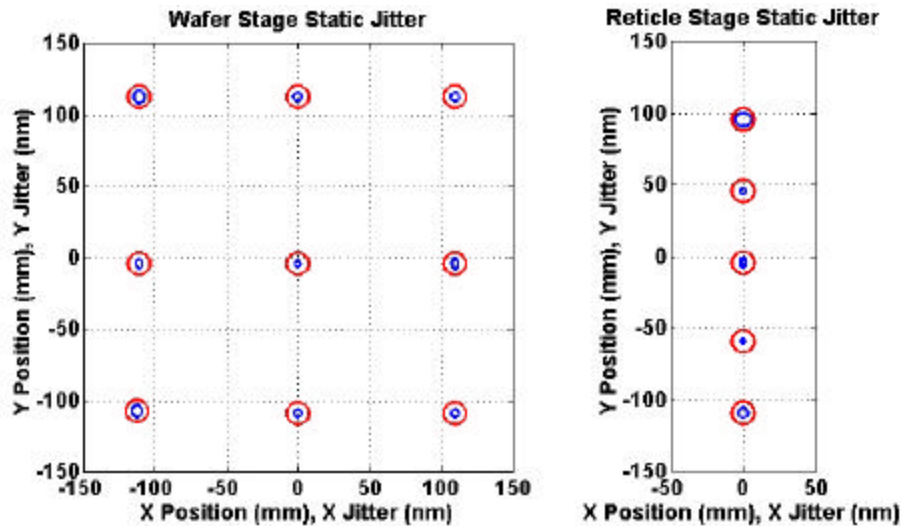

Figure 12. Wafer and reticle stage static stability. The inner ellipses represent the measured jitter. The outer circles represent the specified maximum jitter.
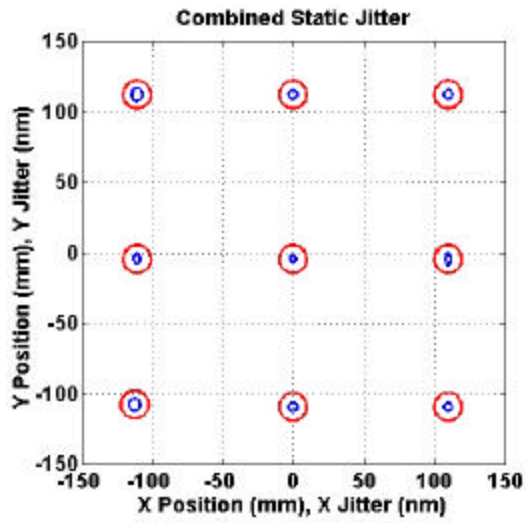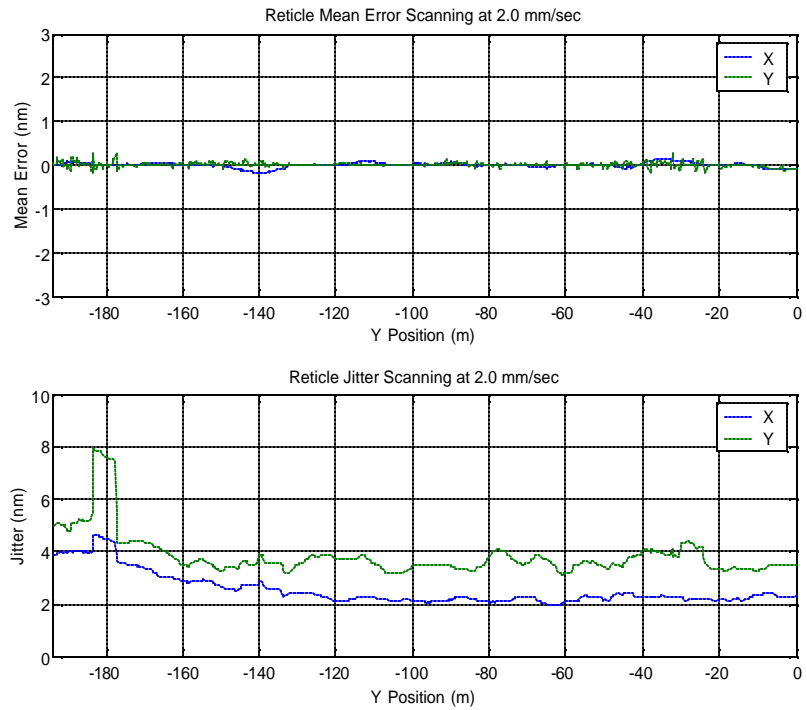
Figure 13. Stage contributions to image blur.

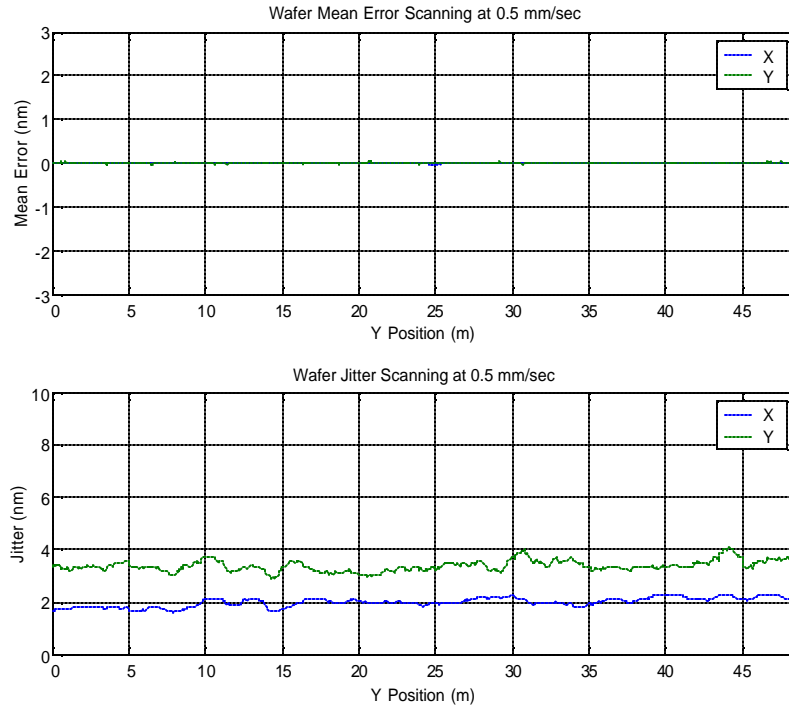Figure 14. Reticle stage scanning performance at 2.0mm/sec.

Figure 15. Wafer stage scanning performance at 0.5 mm/sec.

6. PROJECTION SUBSYSTEM

The developmental set of optics (PO Set 1) is a four-mirror ring-field design, of 0.1 NA and 4× reduction. The projection optics were aligned and characterized using a visible-light interferometer that was constructed to perform wavefront and distortion measurements across the ring field of the projection optics[1]. The interferometer is a single-pass phase-shifting point-diffraction interferometer, in which the reference and test beams are formed by diffraction from pinholes located at the reticle and wafer planes. The pinholes at each of these planes are formed in a metallic film on a glass substrate and are arranged in an array of 45 points to sample the ring field. The relative transverse coordinates of all pinholes were measured to an accuracy of 12 nm using a Leica IPRO mask inspection tool, and the relative z coordinates of the pinholes were determined to 10 nm from an interferometric measurement of the substrate surface. From these data the tilt and focus terms of wavefront measurements can be calibrated to yield image-plane distortion (including absolute magnification) and curvature of field. A full-field set of data is collected sequentially, one field point at a time, returning to a reference field point periodically to track any drift of the pinhole substrates relative to the projection optics. The accuracy of the interferometer is estimated to be better than 0.26 nm rms for wavefront (in the first 36 Zernike polynomials) and 20 nm rms for image-plane distortion. The wavefront accuracy of the interferometer was qualified by comparing results with at-wavelength measurements of PO Box 1[10]. This comparison revealed some systematic errors in the visible-light measurements, the cause of which was subsequently found and corrected. A comparison of the measured wavefront maps at one particular field point is shown in Figure 16. A more detailed comparison between visible and EUV data at 12 field points shows that the mean difference in the two techniques is 0.57 nm in the spatial frequency band up to 40 cycles per pupil diameter, and 0.26 nm in the decomposition into the first 36 Zernike polynomials. Note that rigid-body adjustments of the optics can only affect the first 20 Zernike polynomials, and therefore, to the 0.26 nm level, alignment at visible light is equivalent to alignment at EUV.

l = 532 nm   **l = 13.4 nm**   **difference**

+6nm

-6nm

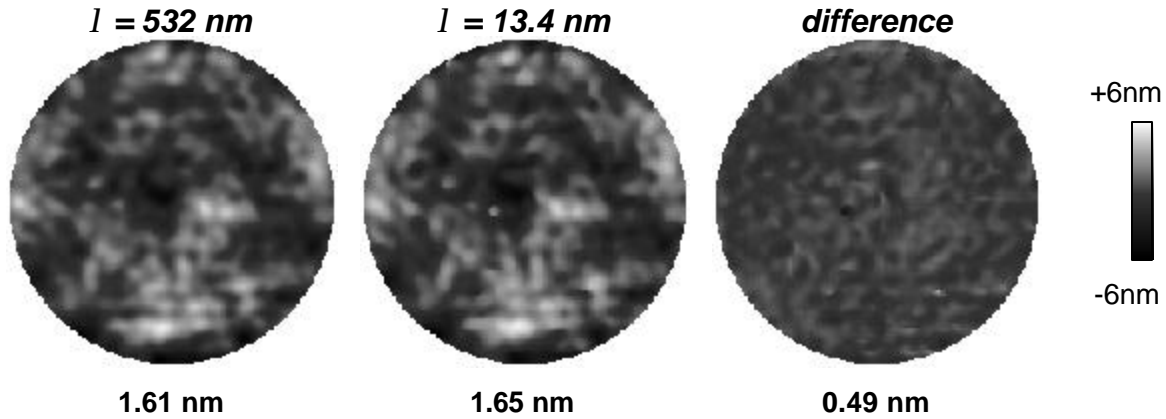**1.61 nm**   **1.65 nm**   **0.49 nm**

Figure 16. Measured wavefront error at the central field point of PO Box 1. Shown are the measurements made in the visible-light interferometer (at a wavelength of 532 nm), in the at-wavelength interferometer (at the EUV wavelength of 13.4 nm) and the point-by-point difference of the wavefront maps. All sets of data are filtered to a maxiumum of 40 cycles across the pupil diameter, and the rms error in this frequency range are 1.61 nm, 1.65 nm, and 0.49 nm respectively.

The projection optics were aligned using a multi-conjugate method[11]. Briefly, this method decomposes the full-field wavefront and distortion data into "misalignment modes" that are characteristic of the projection optics and which vary in sensitivity. The corrections to the positions and tilts of the mirrors of the projection optics are known for each misalignment mode, and so a compounded correction is determined from the amplitude of all sensitive modes. The correction seeks to minimize the rms wavefront error, distortion, and curvature of field, averaged across the field. The correction also includes the tilts and positions of the reticle and wafer planes (i.e. the pinhole planes). Since the locations of these planes are integral to the alignment of the system, this information must be transferred from the alignment interferometer to the ETS. This is achieved by two sets of capacitance sensors and two CCD cameras that are mounted to the projection optics assembly. The sensors determine the distance between the sensor head and the metallic film of the pinhole planes. The tip, tilt, and z displacement of these planes are determined using a set of three capacitance gauges. The in-plane displacement and rotation of the reticle plane is determined using two CCD cameras that view a set of fiducials written on that pinhole plane. When the PO Box is placed in the ETS, the sensors and cameras are used to place the reticle and wafer stages at the correct positions relative to the projection optics.

The final alignment results are shown in Figure 17, which displays a contour plot of the rms wavefront error (in the first 36 Zernike polynomials) across the field and a vector plot of the image distortion. The wavefront error varies from 0.89 nm, near the center of the field, to 1.42 nm at the extremes of the field. The mean wavefront error is 1.20 nm. The mean distortion magnitude is 24 nm. However, the estimated error in the distortion measurement is 20 nm, indicating that, in terms of distortion, the alignment has converged to the measurement.
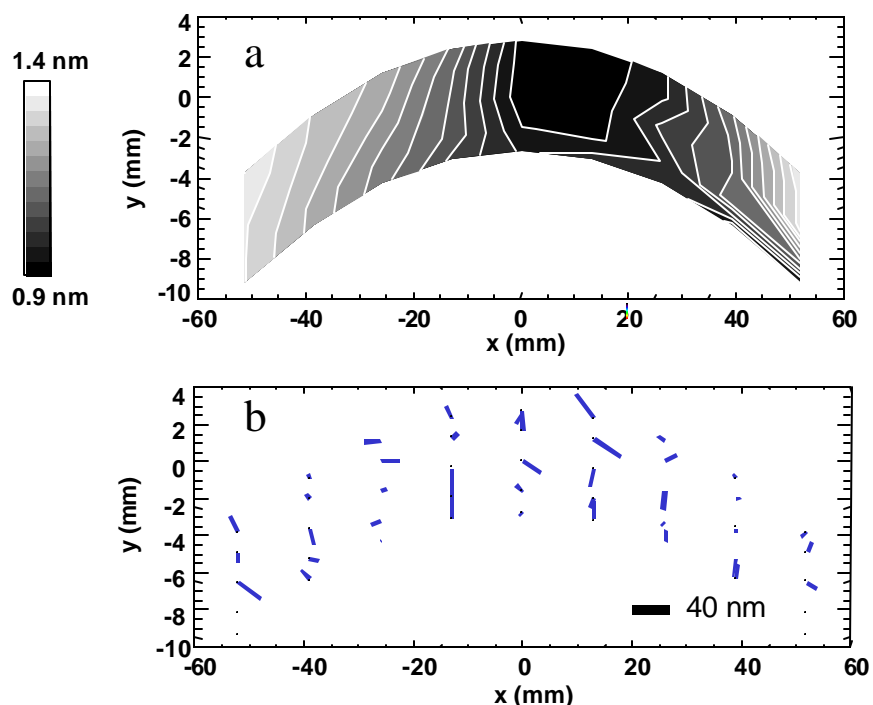
Figure17. (a) Measured rms wavefront error as a function of field location at the mask plane, as measured in the visible-light alignment interferometer, and (b) measured distortion (image placement error).

7. OPTICS FABRICATION

In manufacturing the projection optics substrates for the ETS, significant technical advances were achieved in both their metrology and fabrication. Stringent specifications for the ETS necessitated 3-5x reductions in the rms error levels in both figure and finish beyond the 1996 state-of-the-art, and thus concurrent development programs were begun at the commercial optics manufacturer and within the Metrology Group at LLNL[12]. The development of the Phase-Shifting Diffraction Interferometer (PSDI) at LLNL[13] enabled the measurement of both spherical and aspherical optical surfaces relative to near-perfect spherical waves generated by diffracting a laser beam through a small aperture. Accuracy is assessed using a "first principles" reference to the diffracted spherical wave combined with a detailed analysis of higher order error sources. Interferometers specific to each of the four ETS projection optics were installed at both LLNL and at the supplier site for use in fabrication cycle, validation, and cross-comparisons. The industrial supplier exhibited significant progress in developing their polishing technology with the delivery of a preliminary set of ETS optics (Optics Set 1) which was reported at SPIE in March 2000[1].

Enabling sub-70 nm printing on the ETS requires the completion of a final set of optical substrates (Optics Set 2) to error levels substantially below those obtained for Set 1. Optics Set 2 has been successfully delivered by the optics vendor and demonstrates significant milestones in both metrology and fabrication. Polishing development and upgrades to the PSDI metrology systems proceeded in parallel with substrate manufacturing. Polishing processes aimed at smoothing high frequency roughness generally lead to degradation of figure accuracy, and conversely, processes aimed at meeting figure requirements typically lead to increased roughness. The vendor made important progress in developing methodologies for converging in particular specification categories while minimizing degradation in other categories. This capability is expected to be especially valuable in meeting future specifications for production EUV tools.

Measured rms errors for figure and two categories of surface finish are presented in Table 1 for both the Set 1 and Set 2 optics, as well as the Set 2 specification level. A factor of two improvement in figure errors was achieved for Set 2, which generally meets the specification value of 0.25 nm rms. The spatial frequency range associated with the definition of figure

includes all spatial wavelengths longer than 1 mm. A collage showing the final surface figure measurements of Optics Set 2 made with the PSDI are shown in Figure 18. These particular measurements include contributions from 1) long period errors that contribute to low-order aberrations; 2) higher-order figure errors that are not significantly affected by alignment; and 3) waviness errors that contribute to flare. The category of finish labeled MSFR (Mid-Spatial Frequency Roughness) includes spatial periods between 1 mm and 1 micron and leads to near-angle scattering. The improvement in MSFR and in the higher frequency region of figure will lead to a substantial reduction in flare. Finally, the finish category labeled HSFR (High-Spatial Frequency Roughness) is defined for periods shorter than 1 micron and relates to scattering outside of the optical system and generally represents a throughput loss.

Two fabrication issues caused aspects of the Set 2 optics be slightly out of specification. First, the surface of M2 deformed due to edge machining performed after the final polishing operation, causing figure error level to exceed the specification. Although, this type of deformation was anticipated, the magnitude was larger than expected. Residual stress in the bulk material may have "relaxed" after material in this area was removed. Although the vendor was prepared to make a figure correction, it was deemed unnecessary after detailed modeling of the optical system showed that the error was almost entirely low order and could be compensated during alignment.

The HSFR for Set 2 exceeds the 0.10 nm rms specification by about a factor of 2x. The original specification value was set aggressively at the beginning of the ETS contract to a level that is often obtained on small superpolished flats (Zerodur™). However, during the course of the project, achieving this low level of HSFR has been elusive due to the use of tooling appropriate for curved (aspheric) optics instead of flats. The HSFR levels are generally higher for Set 2, which is an indication of the coupling between the figuring and smoothing operations. The tighter figure specification for Set 2 is achieved with some trade-off from finish. The added roughness will lead to additional throughput loss and be evident as a lower reflectance (1-2%) from the multilayer coating. Since delivering the Set 2 optics, the vendor has demonstrated the ability to attain lower levels of HSFR (~0.15 nm rms on M3). Another category not indicated in Table 1 is

Table 1. Measured and specified values for figure and finish for Optics Set 1 and Optics Set 2.

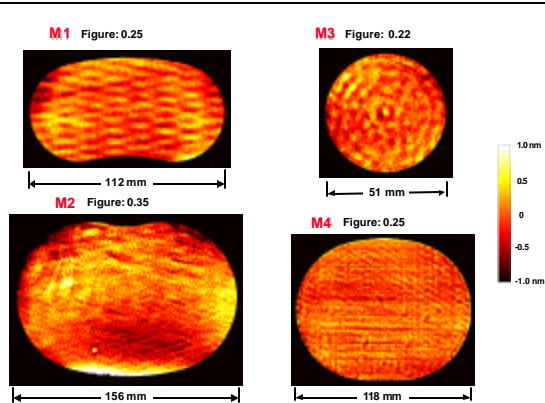| (all units in nm rms)		Set 1	Set 2	Spec
M 1	Figure:	0.40	0.25	0.25
	MSFR:	0.30	0.21	0.20
	HSFR:	0.14	0.24	0.10
M 2	Figure:	0.45	0.35	0.25
	MSFR:	0.25	0.20	0.20
	HSFR:	0.16	0.19	0.10
M 3	Figure:	0.38	0.22	0.25
	MSFR:	0.26	0.15	0.20
	HSFR:	0.17	0.24	0.10
M 4	Figure:	0.49	0.25	0.25
	MSFR:	0.28	0.22	0.20
	HSFR:	0.17	0.17	0.10

Figure 18. Final figure measurements of Optics Set 2 made using the PSDI. Substrates were polished at SVG-Tinlsey (Richmond, CA)

the uniformity of roughness over the substrates, which could impact the uniformity of flare and throughput over the field, and uniformity of illumination over the pupil fill. The section on multilayer coating provides greater detail of this latter point, although the general area of uniformity is still being analyzed.

8. MULTILAYER COATINGS FOR SET 2 PROJECTION OPTICS

Set 2 of the four projection optics (M1, M2, M3, M4) for the ETS has been successfully coated and characterized. All four mirrors were multilayer-coated with Mo/Si during a single deposition run using a new, production-scale DC-magnetron sputtering system (installed at LLNL), described in detail in Ref. 14. Coating simultaneously all optics insures best wavelength matching and maximizes the throughput of the EUVL tool. During multilayer deposition, the Set 2 mirrors were spun around their optical axis and not around the center of their clear aperture, as was the case for the Set 1 optics[15]. The advantage of the Set 2 coating geometry is that all thickness errors are rotationally symmetric around the optical axis and affect all field points in the same way, easing the task of compensating errors in the alignment of the ETS. On the other hand, multilayer thickness has to be controlled to larger radii with the Set 2 coating arrangement, thus, achievement of the desired uniform thickness profile becomes more challenging. Ideally, the multilayer coatings should not degrade the residual wavefront error of the imaging system design and should effectively become "invisible" to the optical performance. For the Set 2 optics, this requirement is equivalent to depositing multilayer coatings which would be uniform in the clear aperture

region to within ±0.2% peak-to-valley (P-V) and add a figure error of less than 0.1 nm rms. (For comparison, the requirements for the Set 1 optics were ±0.25% P-V uniformity and 0.15 nm rms added figure error).

The EUV reflectance of the Set 2 coatings was measured at beamline 6.3.2. of the Advanced Light Source synchrotron at Lawrence Berkeley National Laboratory. Measurements were made at the nominal angles of incidence of each mirror. Wavelengths and reflectance values at each individual point on the optic surface were measured with a 0.002 nm and 0.2% (absolute) precision, respectively. The centroid wavelength was determined for each reflectance curve and the thickness profile for each optic was produced using values of centroid wavelength normalized at an arbitrary point on the optic surface. The P-V thickness uniformity specification of ±0.2% was met for all four coatings. As an example, Figure 19 shows the measurement results for the M2 optic, using data points obtained every 5 mm in the radial direction. The added figure errors due to the multilayer coatings were determined to be 0.032 nm rms (M1), 0.037 nm rms (M2), 0.040 nm rms (M3) and 0.015 nm rms (M4), well within the aforementioned requirement of 0.1 nm rms. The centroid wavelength of each optic, weighted across the clear aperture area, was measured to be 13.355 nm (M1), 13.347 nm (M2), 13.363 nm (M3) and 13.342 nm (M4). This results in an average wavelength of 13.352 nm for the projection optics system, with an outstanding optic-to-optic matching of $1\sigma=0.010$ nm, producing 99.3% of the throughput of an ideally matched four-mirror system. This is an improvement over the wavelength matching of $1\sigma=0.032$ nm achieved for the Set 1 optics. It is mostly due to the fact that all four Set 2 optics were coated during the same deposition run with the new DC-magnetron sputtering tool, while the Set 1 optics had to be coated one at a time due to size limitations of the previous deposition system that was available. The excellent levels of wavelength matching and thickness uniformity achieved for all Set 2 projection mirrors guarantee that the Set 2 multilayer coatings will not introduce any additional aberrations in the imaging performance of the ETS system.
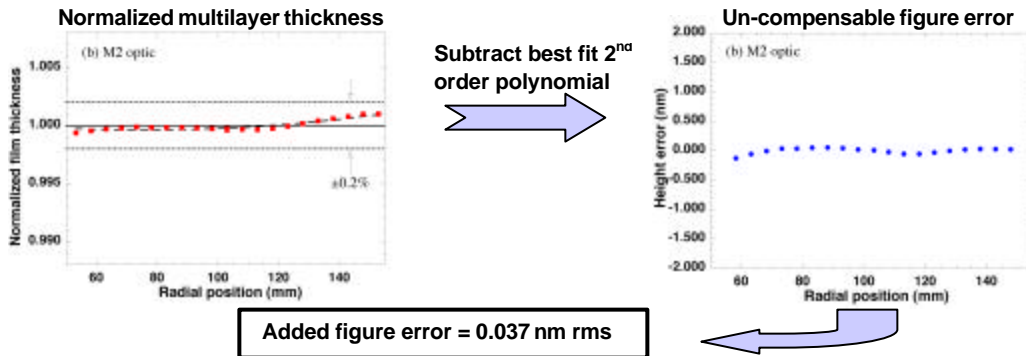

Figure 19. Multilayer profile results vs. radius in the clear aperture area of the M2 optic. The left plot is the normalized film thickness as measured at the ALS synchrotron. A portion of the non-uniformity, corresponding to a best-fit 2nd order polynomial, can be compensated during alignment of the system. The right plot is what remains after subtraction of the polynomial from the curve on the left, expressed in nm units. It represents the un-compensable figure error that the multilayer stack is adding to the system. The multilayer coating is well within specifications in terms of both P-V uniformity and rms added figure error.

Multilayer peak reflectances were measured at 63.8% (M1), 65.2% (M2), 63.8% (M3) and 66.7% (M4) in the center area of the clear aperture of each optic. The variation in reflectance values among the four optics is consistent with their high frequency substrate roughness as verified through atomic force microscopy characterization of the substrates prior to coating (see previous Section) and scattering measurements of the coated optics. In addition to the radial direction shown in Figure 19, reflectance data were obtained in several other directions on each mirror. Significant reflectance variations across the surface were observed for some of the optics. In the case of M2 for instance, reflectance varied by as much as 2.5% within the clear aperture[14]. This effect is a direct result of the high frequency roughness topography of the substrate. Reflectance variations across the surface of a given optic are undesirable since they cause intensity variations ("apodization") in the system exit pupil and may degrade the performance of the imaging system. Calculations using the measured reflectance maps of all four Set 2 projection optics demonstrated that the apodization in the ETS system will be small and can be compensated. In the future, specifications will be set for the substrate finish uniformity of beta-tool and production optics in order to prevent apodization-related problems in the lithographic performance of commercial systems.

9. INITIAL TOOL-SETUP RESULTS

Static images are being printed within the arc-shaped field of view to characterize the image quality and determine tool-setup parameters needed for scanned imaging. First, open frame images are printed to determine the exposure time required to clear the resist. Shipley Co. EUV-2D resist was used for the initial tool setup experiments for several reasons. It has good sensitivity in the EUV, about 5.9 mJ/cm^2 for 100 nm dense lines in 100 nm thick resist. It has been well characterized in the EUV on the 10x microstepper[16]. It has demonstrated good stability in both air and vacuum. The final adjustment of the illuminator is performed using open frame exposures and reticle illumination sensor scans to assure that the six illumination channels are correctly positioned at the reticle. (See Fig. 20) Fine tuning of the illuminator is achieved by tipping and tilting of the C2 assembly and C4 element and by fine positioning of the source.

Figure 20. Open-frame static exposure showing the arc-shaped field of view of the ETS projection system. The arc is 24 mm in length at the wafer.

The next step in tool setup is to find focus at the central field point. The purpose of this step is to determine whether the PO Box has maintained good alignment. Focus/exposures matrices were printed, starting with coarse steps in focus and dose and moving to finer steps as the optimum values are narrowed down. An initial static image at the central field point is shown in Figure 21. The best focus was found to be only 8 microns above the expected location. This result demonstrates that the PO Box image and object plane sensors performed well, and the image-plane location error is within its allocation in the stage range-of-motion budget. The focus is reproducible from wafer to wafer with a total error of 0.25 microns.

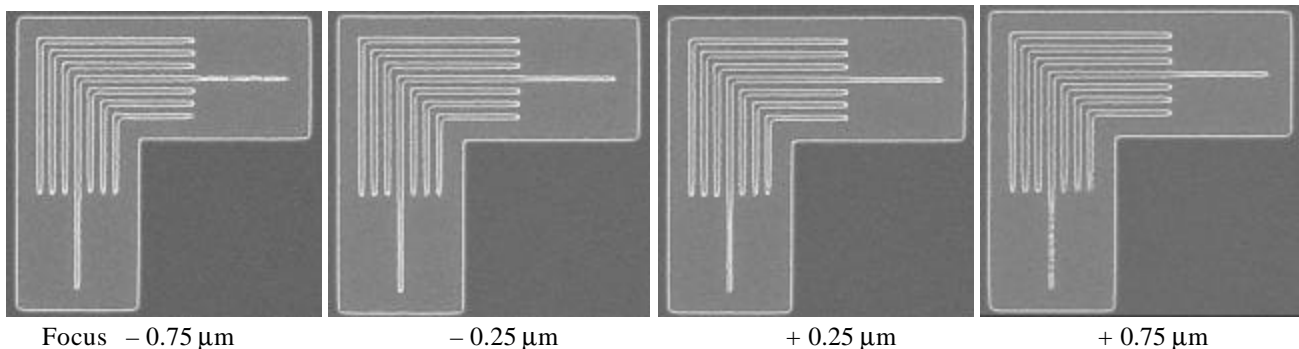| Focus   – 0.75 µm | – 0.25 µm | + 0.25 µm | + 0.75 µm |

Figure 21. Through-focus static images of 150 nm dense and isolated lines in the vertical and horizontal recorded at the central field point on the first day of imaging experiments using the ETS.

The most sensitive aberration to position of the projection mirrors is astigmatism. Careful analysis of the through-focus images reveals a small amount of astigmatism. The best focus position for vertical and horizontal lines differs by about one micron (See Fig. 22). Comparison of these results to simulated images, indicates that the image quality can be improved by a 1 nm rms adjustment in astigmatism. Since this adjustment can be accomplished in situ, the PO Box has clearly demonstrated excellent stability during the 9 months it has been installed in the ETS. During this time the PO Box was removed and installed three times in the course of system integration activities.
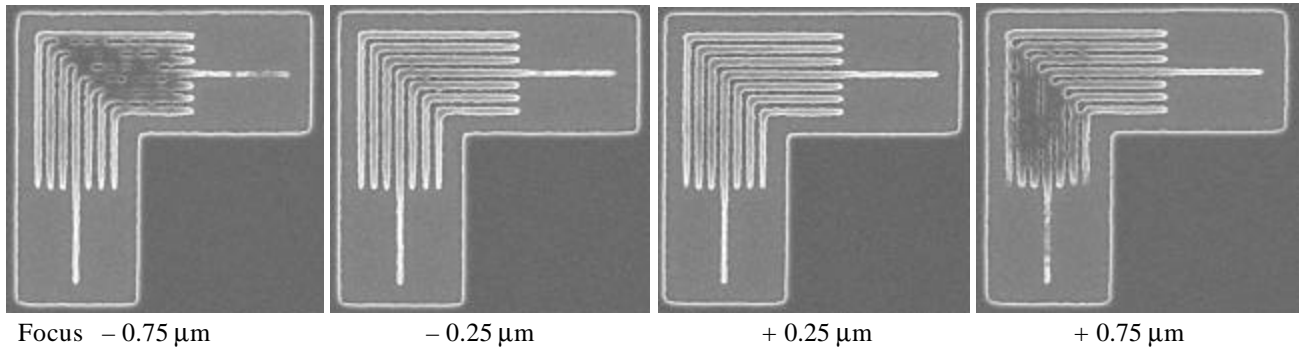
Figure 22 Through–focus images of 100 nm iso/dense elbows at the central field point prior
to correction for astigmatism. The horizontal lines are out of focus in the far-left image,
while the vertical lines remain in focus. The opposite condition is evident in the far-right image.

The model of the projection system indicated that a tilt of 6 micro-radians in the M4 mirror was sufficient to correct for the astigmatism. The indicated adjustment was performed in situ and a subsequent focus-exposure matrix confirmed that the astigmatism correction was successful (See Fig. 23). One hundred nanometer features have been obtained throughout the arc-shaped field of view. This is the largest 100-nm-resolution field demonstrated to date using EUV radiation. Scanning will increase the field size by about 20 fold.
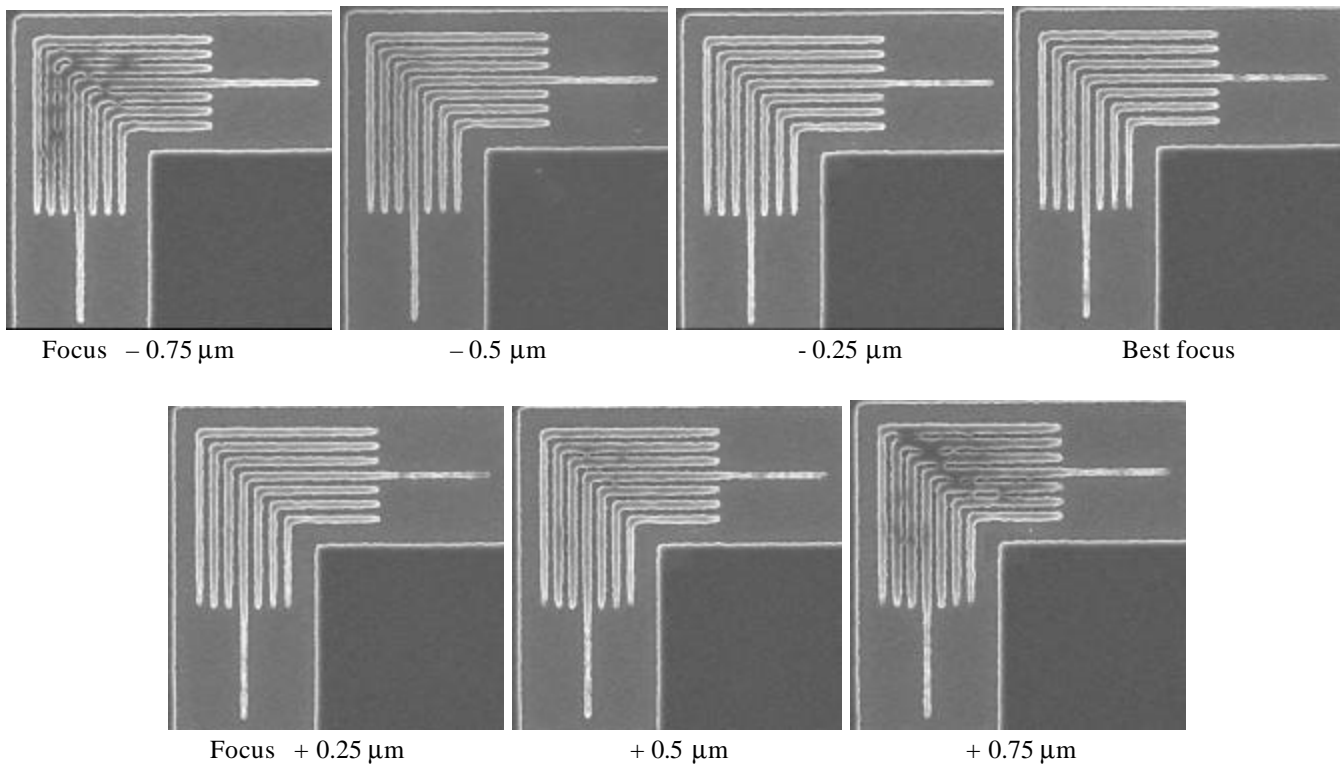

Figure 23 Through-focus images of 100 nm iso/dense elbows at the central field point after
correction for astigmatism. The correction is best seen at 0.75 µm on either side of best focus.
At this point, just outside of the predicted depth of field, the horizontal and vertical lines are
going out of focus together, indicating that the alignment has been optimized with respect to
astigmatism.

The next step in tool setup is to determine stage skew and scan magnification. An accuracy of 5 ppm and 5 microradians, respectively, is required to assure that neither of these parameters contribute significantly to image fade. The scan parameters

are being determined by printing patterns of Leika IPRO marks and analyzing them using an IPRO tool. These experiments are ongoing with the objective of demonstrating scanned images in the near future.

10. SUMMARY

The ETS is operational in static imaging mode, six months ahead of the originally planned operational date. The system is performing as expected and in agreement with modeling results. Static images containing 100 nanometer isolated and dense features have been printed in the largest EUV print field demonstrated to date at this resolution. Stability of the projection system has been demonstrated over a nine-month period during which it was installed three times in the course of system integration. Imaging performance was improved by the correction of 1 nm rms astigmatism, through a small in situ adjustment of the projection system, much the same as is done in advanced optical lithographic systems. Ongoing tool-setup experiments will determine the machine parameters required to demonstrate scanned images in the near future.

These results have been achieved using a developmental projection system, while an improved projection system is being assembled and aligned. The improved system uses a set of mirrors that has been fabricated to tighter tolerances and coated with multilayers to achieve nearly ideal wavelength matching. Upgrades in the other major subsystems are also under development. The source will be upgraded from 40 watts to 1700 watts of drive laser power and from a Xe gas-jet target to a Xe liquid-jet target for improved conversion efficiency. The stage system will be upgraded from aluminum platens to low-thermal-expansion platens, and further stage modifications will enable scan speeds up to 10 mm/s at the wafer.

The performance goal for the ETS in its final configuration is to print 70 nm dense features in scanned images. During the coming year the ETS will continue to deliver major new results in EUVL tool development as upgrades to the projection optics and other subsystems are completed.

ACKNOWLEDGMENTS

REFERENCES

1. D. A. Tichenor, G. D. Kubiak, W. C. Replogle, L. E. Klebanoff, J. B. Wronosky, L. C. Hale, H. N. Chapman, J. S. Taylor, J. A. Folta, C. Montcalm, R. M. Hudyma, K. A. Goldberg, and P. Naulleau, "EUV Engineering Test Stand," *Emerging Lithographic Technologies IV*, Proceeding of SPIE Vol. 3997, 48-69, (2000).
2. L. C. Hale, R. M. Hudyma, J. S. Taylor, R. L. Thigpen, and C. A. Jung, "High-NA Camera for an EUVL Microstepper," Proceedings of the American Society for Precision Engineering, Vol. 22, 521-524 (2000).
3. K. A. Goldberg, P. Naulleau, P. J. Batson, P. Denham, E. H. Anderson, J. Bokor, and H. N. Chapman, "EUV Interferometry of a Four-Mirror Ring-field EUV Optical System," *Emerging Lithographic Technologies IV*, Proceeding of SPIE Vol. 3997, 867-873, (2000).
4. L. E. Klebanoff, M. E. Malinowski, P. Grunow, W. M. Clift, C. Steinhaus, A. H. Leung, and S. J. Haney, "First Environmental Data from the EUV Engineering Test Stand," these *Proceedings.*
5. G. D. Kubiak, L. J. Bernardez, K. Krenz, and W. C. Sweatt, "Scale-up of a Cluster Jet Laser Plasma Source for Extreme Ultraviolet Lithography", Proceedings of the SPIE Vol. 3676, 669 (1999).
6. P. Celliers, L. B. Da Silva, C. B. Dane, S. Mrowka, M. Norton, J. Harder, L. Hackel, D. L. Matthews, H. Fiedorowicz, A. Bartnik, J. R. Maldonado, and J. A. Abate, "Optimization of X-ray Sources for Proximity Lithography Produced by a High Average Power Nd:glass Laser," J. Appl. Phys. **79**, 8258 (1996).
7. J. Blackburn, P. K. Carroll, J. Costello, and G. O'Sullivan, "Spectra of Xe VII, VIII, and IX in the Extreme Ultraviolet: 4d-mp, nf Transitions," J. Opt. Soc. Am. **73**, 1325 (1983).
8. B. A. Hansson, M. Berglund, O. Hemberg. H. M. Hertz, "Xenon liquid-jet laser-plasma source for EUV lithography," SPIE Conference on Microlithography, Santa Clara, CA, February (2001).
9. J. B. Wronosky, T. G. Smith, M. J. Craig, B. R. Sturgis, J. R. Darnold, D. K. Werling, M. A. Kincy, D. A. Tichenor, M. E. Williams, P. Bischoff, "Wafer and Reticle Positioning System for the Extreme Ultraviolet Lithography Engineering Test Stand," in *Emerging Lithographic Technologies IV*, Proceedings of SPIE Vol. 3997, 829-839 (2000).

10. K. A. Goldberg, P. Naulleau, P. J. Batson, P. Denham, E. H. Anderson, J. Bokor, and H. N. Chapman, "EUV Inteferometry of a Four-Mirror Ring-Field EUV Optical System," *Emerging Lithographic Technologies IV*, Proceeding of SPIE Vol. 3997, 867-873, (2000).

11. H. N. Chapman and D. W. Sweeney, "A Rigorous Method for Compensation Selection and Alignment of Microlithographic Optical Systems," Proceedings of SPIE Vol. 3331, 102–113 (1998).

12. J. S. Taylor, G. E. Sommargren, D. W. Sweeney, and R. M. Hudyma, "The Fabrication and Testing of Optics for EUV Projection Lithography," *Emerging Lithographic Technologies II*, Proceedings of SPIE Vol. 3331, pp. 580-590 (1998).

13. G. E. Sommargren, D. W. Phillion, E. W. Campbell, "Sub-nanometer interferometry for aspheric mirror fabrication," from Precision Science and Technology for Perfect Surfaces, Proc. Of the 9th International Conference on Precision Engineering (9th ICPE), Aug. 29-Sep. 1, 1999, Osaka, Japan, JSPE Publication Series No. 3.

14. R. Soufli, E. Spiller, M. A. Schmidt, J. C. Davidson, R. F. Grabner, E. M. Gullikson, B. B. Kaufmann, S. L. Baker, H. N. Chapman, R. M. Hudyma, C. C. Walton, C. Montcalm, and J. A. Folta, "Multilayer optics for an extreme ultraviolet lithography tool with 70 nm resolution," this Conference Proceedings.

15. C. Montcalm, R. F. Grabner, R. M. Hudyma, M. A. Schmidt, E. Spiller, C. C. Walton, M. Wedowski, and J. A. Folta, "Multilayer coated optics for an alpha-class extreme ultraviolet lithography system," in *EUV, X-Ray, and Neutron Optics and Sources*, S. P. Vernon and K. Goldberg, Eds. Proceedings of SPIE Vol. 3767, 210-216 (1999).

16. R. L. Brainard, C. Henderson, J. Cobb, V. Rao, J. F. Mackevich, U. Okoroanyanwu, S. Gunn, J. Chambers, and S. Connolly, "Comparison of the Lithographic Properties of Positive Resists Upon Exposure to Deep- and Extreme-Ultraviolet Radiation," 43rd *International Conference on Electron, Ion, and Photon Beam Technology and Nanofabrication*, 3384-3389 (1999).